



Muscle degeneration in chronic massive rotator cuff tears of the shoulder: Addressing the real problem using a graphene matrix

Nikoo Saveh Shemshaki^{a,b,c}, Ho-Man Kan^{a,b}, Mohammed Barajaa^{a,b,c}, Takayoshi Otsuka^{a,b} , Amir Lebaschi^d, Neha Mishra^{e,f}, Lakshmi S. Nair^{a,b,c,d,g}, and Cato T. Laurencin^{a,b,c,d,g,h,1} 

Contributed by Cato T. Laurencin; received May 10, 2022; accepted June 21, 2022; reviewed by Edward Botchwey and Raphael Lee

Massive rotator cuff tears (MRCTs) of the shoulder cause disability and pain among the adult population. In chronic injuries, the tendon retraction and subsequently the loss of mechanical load lead to muscle atrophy, fat accumulation, and fibrosis formation over time. The intrinsic repair mechanism of muscle and the successful repair of the torn tendon cannot reverse the muscle degeneration following MRCTs. To address these limitations, we developed an electroconductive matrix by incorporating graphene nanoplatelets (GnPs) into aligned poly(l-lactic acid) (PLLA) nanofibers. This study aimed to understand 1) the effects of GnP matrices on muscle regeneration and inhibition of fat formation *in vitro* and 2) the ability of GnP matrices to reverse muscle degenerative changes *in vivo* following an MRCT. The GnP matrix significantly increased myotube formation, which can be attributed to enhanced intracellular calcium ions in myoblasts. Moreover, the GnP matrix suppressed adipogenesis in adipose-derived stem cells. These results supported the clinical effects of the GnP matrix on reducing fat accumulation and muscle atrophy. The histological evaluation showed the potential of the GnP matrix to reverse muscle atrophy, fat accumulation, and fibrosis in both supraspinatus and infraspinatus muscles at 24 and 32 wk after the chronic MRCTs of the rat shoulder. The pathological evaluation of internal organs confirmed the long-term biocompatibility of the GnP matrix. We found that reversing muscle degenerative changes improved the morphology and tensile properties of the tendon compared with current surgical techniques. The long-term biocompatibility and the ability of the GnP matrix to treat muscle degeneration are promising for the realization of MRCT healing and regeneration.

graphene | muscle degeneration | rotator cuff tears | fat accumulation

Massive rotator cuff tears (MRCTs) of the shoulder are one of the most common injuries related to tendons and muscles in the adult population (1–8). More than 200,000 rotator cuff (RC) repair procedures take place in the United States annually, and that number is expected to increase as a result of the aging US population (1–12). The long duration between rotator cuff tear injury and surgical repair can be described as chronic rotator cuff tendon tear injury and is a commonly observed challenge. The tendon and muscle retraction over months in chronic MRCTs are associated with a set of degenerative changes that include muscle atrophy, fat accumulation, and fibrosis formation (13–18). The regeneration potential of muscle cells provides an intrinsic repair mechanism for minor injuries and damage. However, this repair mechanism cannot reverse the muscle degenerative changes after MRCTs (19–21). Even with the successful repair of the torn tendon, fat accumulation and muscle atrophy are not known to be reversible (4, 7, 11, 17, 22–28).

Despite improvements in surgical procedures and postoperative rehabilitation, muscle degenerative changes increase the retear rate (up to 94%) after successful RC repair (3, 4, 11, 29–34). The limitations of current clinical treatments motivate regenerative engineering approaches to treat muscle degeneration. This study presents a regenerative engineering method as an alternative approach for patients with chronic MRCTs.

Skeletal muscle is a highly aligned tissue that fosters alignment and migration of cells along the direction of tissue fibers (35–39). Studies have demonstrated that the aligned topography of engineered matrices can significantly induce cellular elongation, alignment, and differentiation and guide cell migration along the direction of the matrix (10, 35, 36, 38–43). Graphene-based materials are characterized by their outstanding mechanical properties, high electrical conductivity, and chemical stability (44). Graphene can be combined with a wide range of materials to engineer structures with desired characteristics (45–51). These extraordinary properties make graphene a compelling candidate for tissue regeneration (44, 52–54).

Significance

Currently, patients with rotator cuff tears associated with fat accumulation and muscle atrophy suffer from a high retear rate after rotator cuff repair. The development of new treatments to reverse these degenerative changes may significantly reduce the rate of retear and obviate the need for ultimate shoulder replacement surgery. This paper describes the effects of a GnP matrix that enhances muscle regeneration and reduces fat formation *in vitro*. This paper also shows the efficacy of the implantation of the GnP matrix in reducing fat accumulation, muscle atrophy, and fibrosis formation following chronic MRCTs in a rat model. This study showed the potential of the GnP matrix to be used in a clinical setting to reverse muscle degenerative changes following MRCTs.

Author contributions: N.S.S., L.S.N., and C.T.L. designed research; N.S.S., H.-M.K., M.B., T.O., and A.L., performed research; N.S.S., T.O., N.M., L.S.N., and C.T.L. analyzed data; and N.S.S., H.-M.K., T.O., L.S.N., and C.T.L. wrote the paper.

Reviewers: E.B., Georgia Institute of Technology; and R.L., Biological Sciences Division, University of Chicago.

Competing interest statement: University of Connecticut has filed a patent entitled “Graphene-Based Nanofibers for Skeletal Muscle Tissue Regeneration” on behalf of the inventors, N.S.S. and C.T.L. C.T.L. has the following competing financial interests: Biorez, Globus, HOT, HOT Bone, Kuros Bioscience, NPD, and Cobb (W. Montague) NMA Health Institute. L.S.N. has the following competing financial interests: Biorez.

Copyright © 2022 the Author(s). Published by PNAS. This article is distributed under [Creative Commons Attribution-NonCommercial-NoDerivatives License 4.0 \(CC BY-NC-ND\)](https://creativecommons.org/licenses/by-nc-nd/4.0/).

¹To whom correspondence may be addressed. Email: Laurencin@uchc.edu.

This article contains supporting information online at <http://www.pnas.org/lookup/suppl/doi:10.1073/pnas.2208106119/-DCSupplemental>.

Published August 8, 2022.

Several studies have indicated that electroconductive materials can significantly promote myoblast proliferation and differentiation, even without the use of external electrical stimulation (39, 42, 45, 55). Muscle is an electrically excitable tissue, thus with the combination of conductive material, the aligned structure may serve as a critical cue to facilitate myoblast communication, growth, and development (21, 42, 45, 56).

Studies have shown that high concentrations of calcium ions stimulate myogenesis while reducing intracellular calcium levels, and this can significantly inhibit myoblast differentiation (57) and proliferation (58). Electroactive materials may be responsible for increasing intracellular calcium levels (55). Moreover, a graphene matrix may have an inhibitory effect on lipid formation (59, 60). These effects provide strong motivations for using graphene matrices for reducing fat formation after massive rotator cuff tendon tears.

In this study, we utilized an aligned nanofibrous structure composed of graphene nanoplatelets (GnPs) and poly(L-lactic acid) (PLLA) to induce muscle regeneration and reduce fat accumulation, muscle atrophy, and fibrosis formation. The development of this matrix promises to have an important

beneficial clinical impact, where muscle atrophy and fat accumulation are addressed in the setting of massive rotator cuff tendon tears.

Results

Morphology and Characterization of Aligned GnPs/PLLA Nanofibers. The aligned GnP/PLLA (GnP) matrix was fabricated by electrospinning (Fig. 1A). The representative SEM images (Fig. 1B) show the diameter of nanofibers at different matrices. Fig. 1C shows the average diameters of all nanofibers with GnP concentration. There were no significant differences in the average diameters among different GnP concentrations (Fig. 1C). PLLA nanofibers exhibited increased surface conductivities with the increase of GnPs concentrations (Fig. 1D).

Myoblasts Biocompatibility and Differentiation. All the matrices supported the cell viability and growth of C₂C₁₂ myoblasts after 1, 7, and 14 d in growth media (GM) (Fig. 1E). The cells formed aligned layers along the fibers. All GnP matrices induced C₂C₁₂ myoblasts to express MyoD and MyoG in both

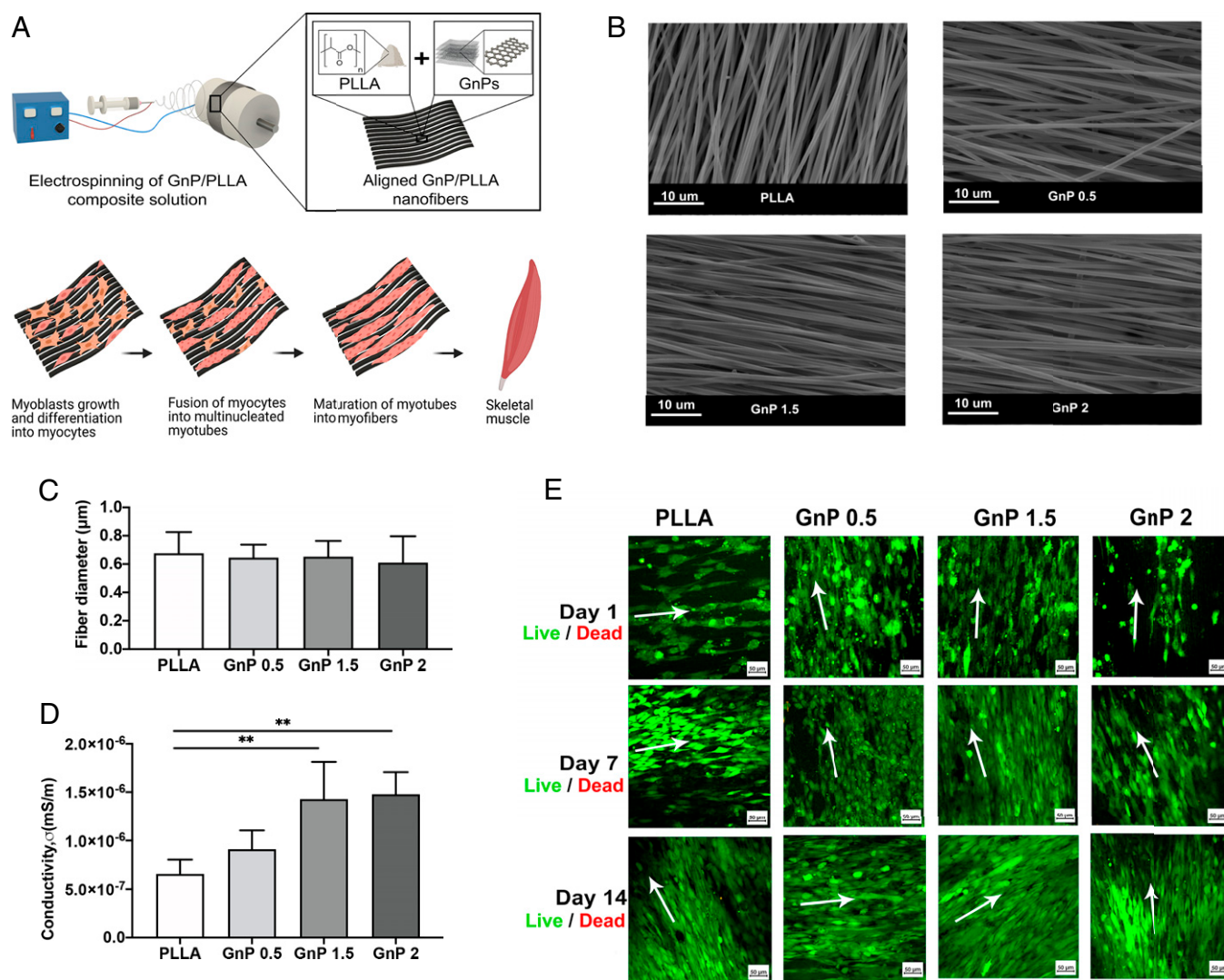


Fig. 1. (A) Schematic illustration of the fabrication process of the GnP matrix. (B) SEM images of the aligned nanofibers. (C) Mean diameter of the electrospun nanofibers ($n = 50$). The average diameters of the aligned nanofibers were 676.7 ± 149.1 nm, 645.3 ± 91.84 nm, 652.6 ± 110.8 nm, and 610 ± 186.1 nm for PLLA, GnP 0.5, 1.5, and 2, respectively. (D) Surface conductivities of the aligned matrices (** $P \leq 0.01$). (E) Live/dead fluorescent images of cell-seeded matrices with aligned orientation after 1, 7, and 14 d (green, viable cells; red, dead cells). Arrows show the main directions of nanofiber alignment.

GM and differentiation media (DM) after 3 and 5 d (*SI Appendix, Fig. S5*).

Further, myotube formation was confirmed by myosin heavy chain (MHC) staining, showing all matrices could induce C₂C₁₂ to form multinucleated myotubes (Fig. 2 *A* and *C*). Fig. 2 *B* and *D* shows the quantification of myotube formation and maturation by calculating the length, fusion, and maturation indices of the fused myotubes. The differentiation indices of the myotubes on the aligned GnP 1.5 were significantly greater than other matrices. The GnP 1.5 demonstrated the longest myotube length compared with PLLA. In addition, the alignment of the fibers and the presence of graphene significantly induced the fusion and maturation of the formed myotubes. Fig. 2 *E–G* shows the comparison of myotube length, fusion, and maturation indices between GnP 1.5 and PLLA in GM and DM, suggesting the GnP matrix itself possesses the ability to induce myoblast differentiation. We will utilize GnP 1.5 in the following study as an optimized GnP matrix.

The Underlying Mechanisms of Graphene in Enhancing Skeletal Muscle Regeneration. We hypothesized that increased myotube formation was attributed to improved intracellular calcium levels induced by the GnP matrix. Fig. 3 shows the calcium imaging of C₂C₁₂ on both PLLA and GnP 1.5 matrices. The results indicated increased fluorescence intensity of Fluo 4-AM in myoblasts on the GnP matrix compared to PLLA at days 1 and 3 in GM. Furthermore, the cells in DM increased the calcium levels compared to GM and increased fluorescence intensity can be observed for both matrices after 3 d in DM. The Fluo-4 AM intensities on GnP and PLLA matrices were similar at day 7 in both GM and DM. GnP showed lower intensity on day 7 compared with day 3.

The Efficacy of Graphene in Reducing Adipogenesis In Vitro. Next, the effect of graphene on adipogenic differentiation in adipose-derived stem cells (ADSCs) was evaluated. Both matrices supported the cell viability of rat ADSCs and no differences were observed between GnP and PLLA at day 3 in GM (*SI Appendix, Fig. S6*). Adipogenic media were introduced to induce adipogenic differentiation on day 3. Fig. 4*B* shows there is no significant difference of cell viability on both matrices after 12 d in the adipogenic medium. The formation of lipid droplets was detected and quantified by Oil Red O staining on day 12 on both GnP and PLLA matrices (Fig. 4 *C* and *D*). GnP showed a significantly lower absorbance than PLLA.

The Efficacy of the GnP Matrix in Reducing Muscle Atrophy and Fat Accumulation in a Rat Chronic MRCT Model. We next investigated the efficacy of the implantation of the GnP matrix in a rat model of chronic MRCTs. At 16 wk after the tendon resection, tendons were sutured back to repair and the GnP matrix was implanted (*SI Appendix, Figs. S1 and S2*). All operated rats had normal activity after the surgery and no problems associated with the surgery, such as infection, were observed during the study. The surgical sites were intact and no tendon rerupturing was observed at both harvesting time points. Gross examination of the supraspinatus and infraspinatus muscles showed obvious muscle atrophy and retraction compared to normal muscle (*SI Appendix, Fig. S9*).

Fig. 5*A* shows the hematoxylin and eosin (H&E) and trichrome staining images of the infraspinatus muscles at 24 wk. N-24, NR-24, S-24, and G-24 indicate the native group, no repair group, suture repair group, and GnP matrix groups at

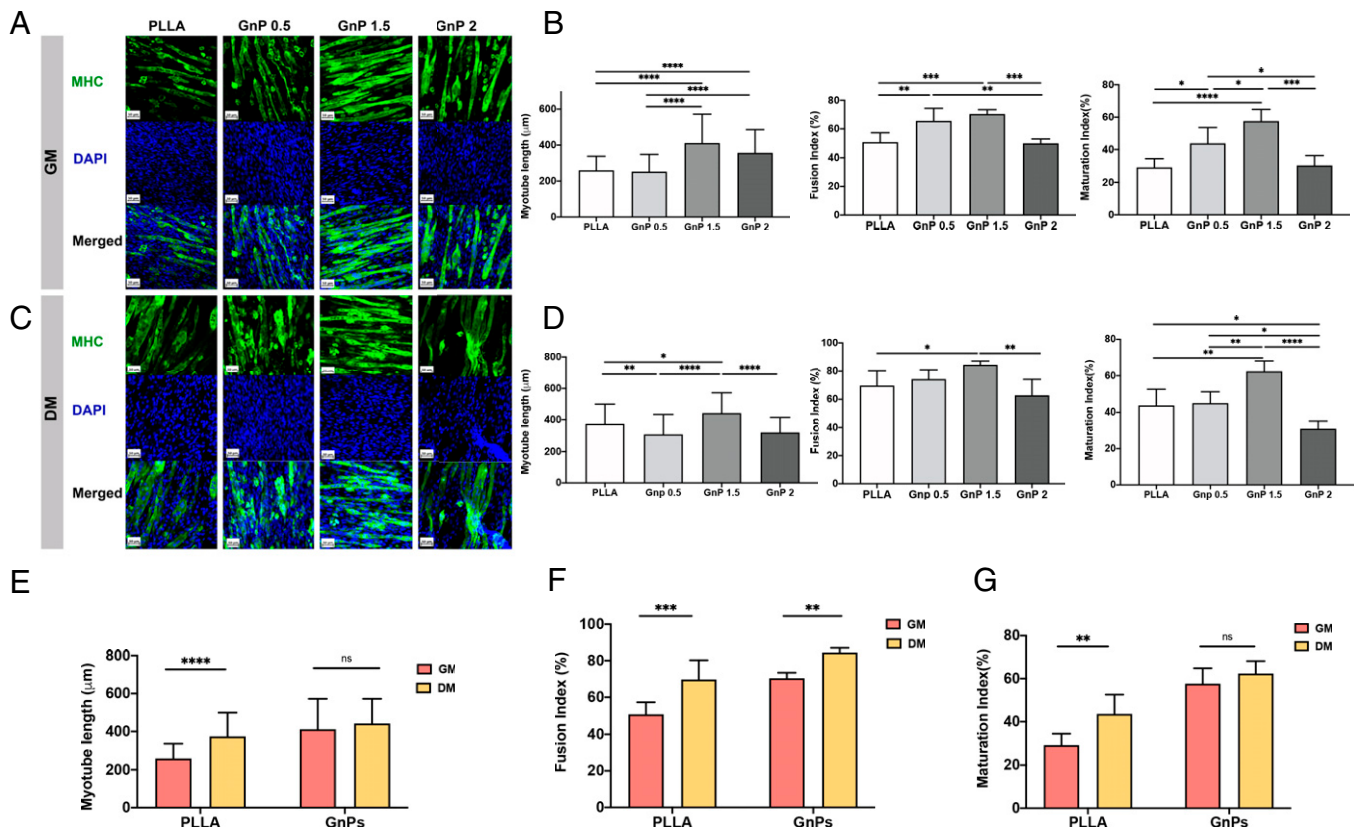


Fig. 2. (A) Immunofluorescent images of differentiated myotubes after 7 d on aligned matrices in GM immune-stained for MHC (green) and nucleus (blue). (B) Quantification of myotube length, fusion index, and maturation index of differentiated myotubes after 7 d on aligned matrices in GM. (C) Immunofluorescent images of differentiated myotubes after 7 d on aligned matrices in DM immune-stained for MHC and nucleus. (D) Quantification of myotube length, fusion index, and maturation index of differentiated myotubes after 7 d on aligned matrices in DM. Comparison of (E) myotube length, (F) fusion index, (G) maturation index between PLLA and GnP 1.5 in both GM and DM, (ns = $P > 0.05$, * $P \leq 0.05$, ** $P \leq 0.01$, *** $P \leq 0.001$, **** $P \leq 0.0001$).

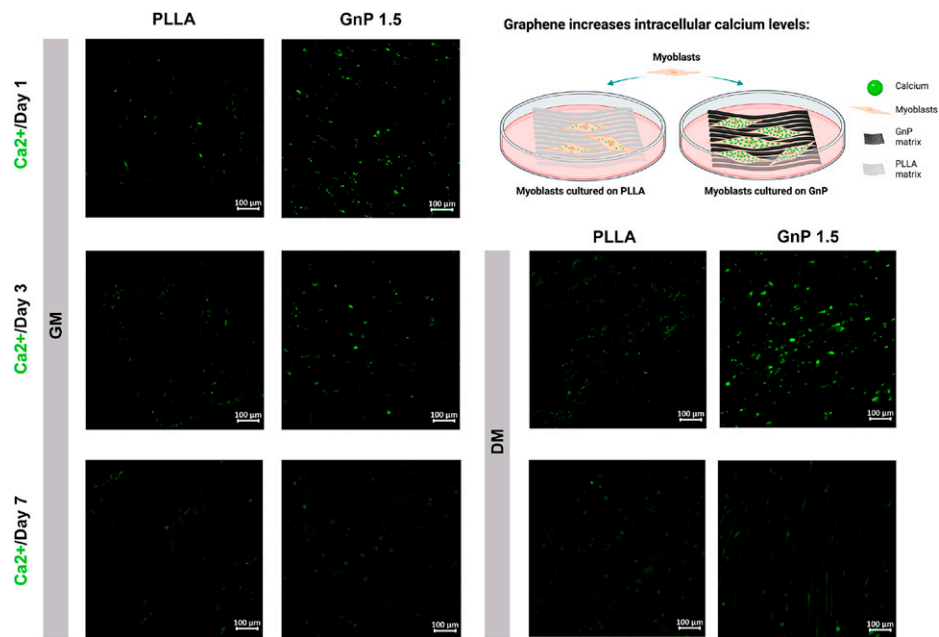


Fig. 3. Calcium imaging of C_2C_{12} myoblasts on the matrices at days 1, 3, and 7 after cell culturing in both GM and DM. Schematic image showing the effects of the GnP matrix on the concentration of intracellular calcium ions.

24 wk, respectively. The fibrosis percentage significantly reduced after the repair surgery; however, there are no significant differences between S-24 and G-24 (Fig. 5B). In the infraspinatus muscle, the fat accumulation grading for G-24 is statistically lower than that for NR-24, but there was no statistically significant difference between S-24 and G-24 (Fig. 5C). At 24 wk, there is a significant difference between NR-24 ($16.11 \pm 4.83\%$) and G-24 ($5.13 \pm 7.57\%$) in infraspinatus muscle mass reduction. Although both S-24 and G-24 showed a lower level of muscle atrophy grading compared with NR-24, no statistically significant differences were observed (Fig. 5D). Of note, G-24 showed a lower degree of muscle atrophy grade compared to S-24 but did not show a statistically significant difference (Fig. 5D).

The effects of GnP matrix implantation in the supraspinatus muscle revealed similar trends with the infraspinatus muscles.

Fig. 5E shows the histological images of the supraspinatus muscles at 24 wk. NR-24 showed the significant formation of fibrosis in supraspinatus muscle compared with N-24 and both repaired groups (Fig. 5F). The fibrosis percentage significantly reduced after the repair surgery in the repaired groups. However, there were no statistically significant differences between the suture repair and GnP matrix repair. The fat accumulation grading in the supraspinatus muscle was significantly lower in G-24 compared with NR-24, but there was no statistically significant difference between S-24 and G-24 (Fig. 5G). The muscle atrophy evaluation shows no statistically significant differences between the repair groups and NR-24, or between S-24 and G-24 (Fig. 5H). Although NR-24 showed the highest supraspinatus mass reduction compared with the S-24 and G-24, no statistically significant differences were observed.

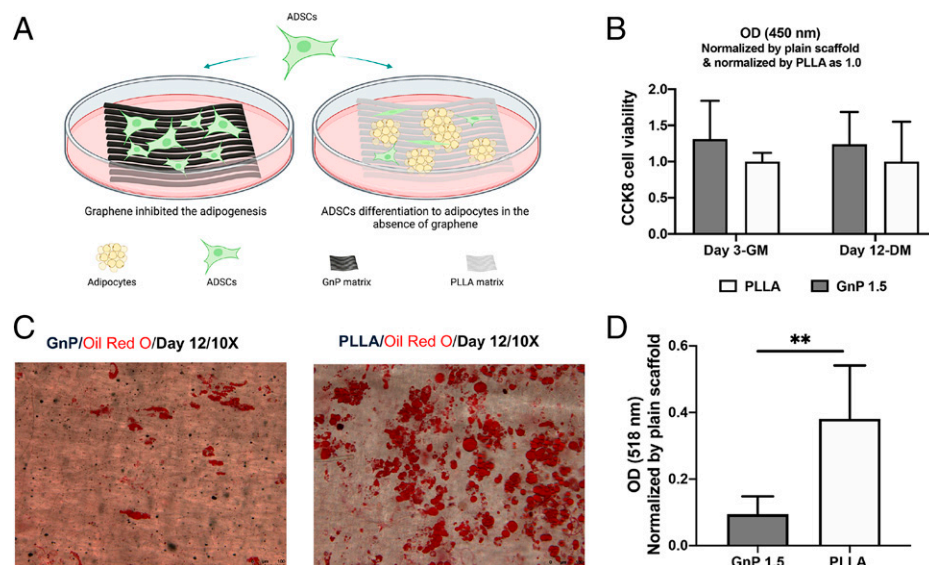


Fig. 4. (A) Schematic illustration of the lipid droplets on GnP 1.5 and PLLA matrices after 12 d of adipogenic induction. (B) CCK8 cell viability on both matrices at day 3 in GM and day 12 in DM. (C) Representative images of the stained lipid droplets on the matrices after 12 d of adipogenic induction. (D) Quantification of the stained lipid droplets was conducted by eluting the Oil Red O stain and measuring absorbance at 510 nm. The readings were normalized to the plain matrix (** $P \leq 0.01$).

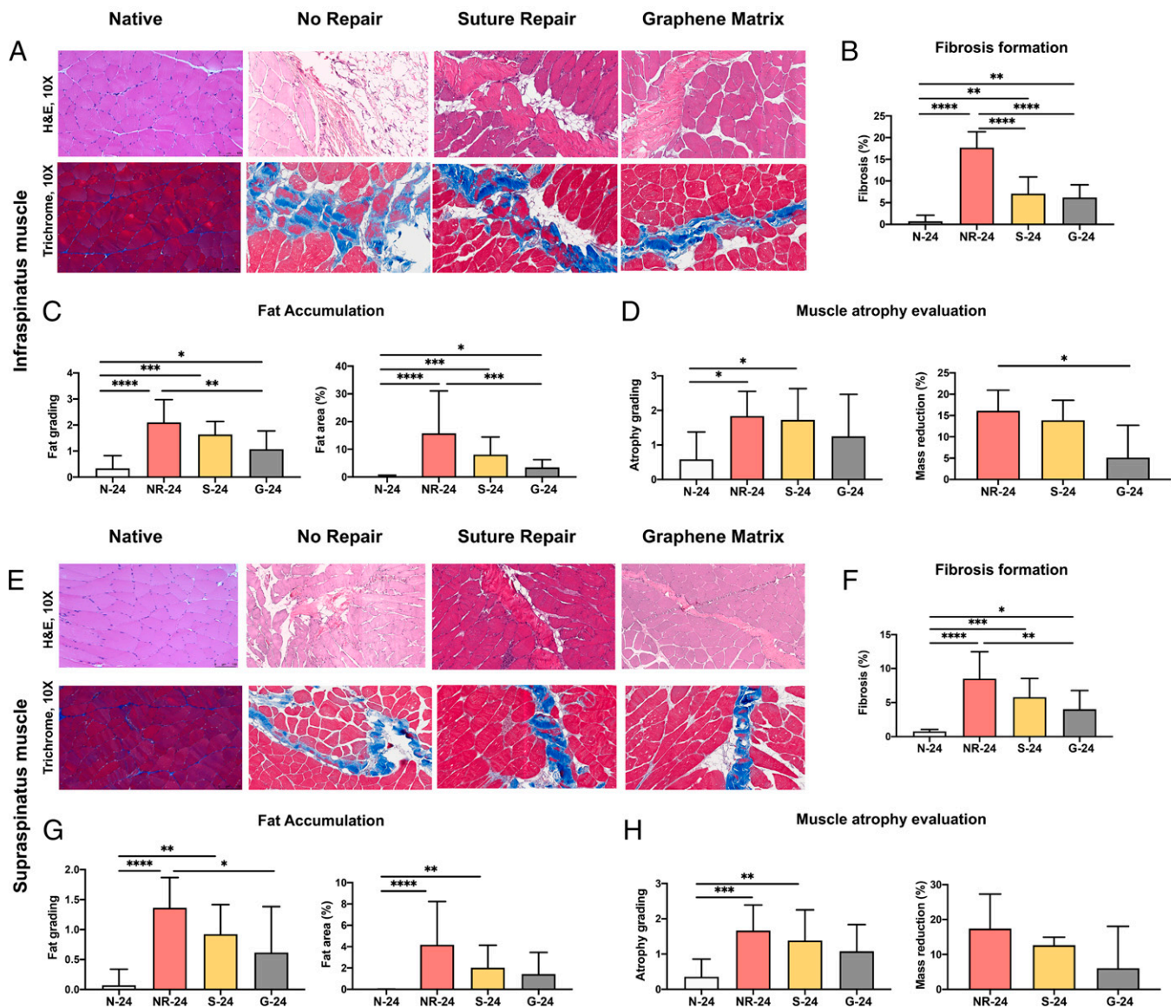


Fig. 5. (A) Representative histological images of infraspinatus muscle at 24 wk. The H&E and trichrome staining of cross-sections of the infraspinatus muscles used for the quantification of (B) fibrosis formation, (C) fat accumulation, and (D) muscle atrophy evaluation for different groups at 24 wk. (E) Representative histological images of supraspinatus muscle at 24 wk. The H&E and trichrome staining of cross-sections of the supraspinatus muscles used for the quantification of (F) fibrosis formation, (G) fat accumulation, and (H) muscle atrophy evaluation for different groups at 24 wk. (* $P \leq 0.05$, ** $P \leq 0.01$, *** $P \leq 0.001$, **** $P \leq 0.0001$).

The GnP matrix boosted its therapeutic effects by the long-term implantation. Fig. 6A shows the histological images of infraspinatus muscles at 32 wk. N-32, NR-32, S-32, and G-32 indicate the native group, no repair group, suture repair group, and GnP matrix groups at 32 wk, respectively. The fibrosis in the infraspinatus muscle significantly reduced for G-32 compared to NR-32 and S-32 (Fig. 6B). The implantation of the GnP matrix also significantly reduced the fat accumulation compared to the NR-32 and S-32 groups (Fig. 6C). As shown in Fig. 6D, a significant reduction of atrophy grading was observed in G-32 compared with NR-32 and S-32 (Fig. 6D). Besides, the mass reduction percentage of infraspinatus muscle was $20.66 \pm 5.17\%$, $20.36 \pm 4.09\%$, and $1.36 \pm 6.48\%$ for NR-32, S-32, and G-32 groups, respectively. G-32 showed statistically significant differences with NR-32 and S-32.

Once again, the GnP matrix implantation brought significant effects on the supraspinatus muscles. Fig. 6E shows the histological

images of supraspinatus muscles at 32 wk. The reduction of the fibrosis rate in G-32 was found compared to NR-32 (Fig. 6F). The fat accumulation grading and fat area percentages of supraspinatus muscle at 32 wk showed statistically significant differences between G-32 and NR-32. (Fig. 6G). The atrophy grading showed a significant reduction in muscle atrophy of G-32 compared with NR-32 and S-32 at 32 wk. Similarly, the mass reduction percentage of supraspinatus muscle was $24.14 \pm 12.56\%$, $23.45 \pm 11.25\%$, and $4.92 \pm 5.01\%$ for NR-32, S-32, and G-32 groups, respectively. G-32 showed statistically significant differences with NR-32 and S-32.

Overall, histological analysis showed GnP matrix implantation induced a reversal of muscle degeneration (SI Appendix, Table S1). Notably, there were no statistically significant differences of all measured parameters (fibrosis formation, fat accumulation, and muscle atrophy) between the native group and GnP matrix group at 32 wk in both infraspinatus and supraspinatus muscles.

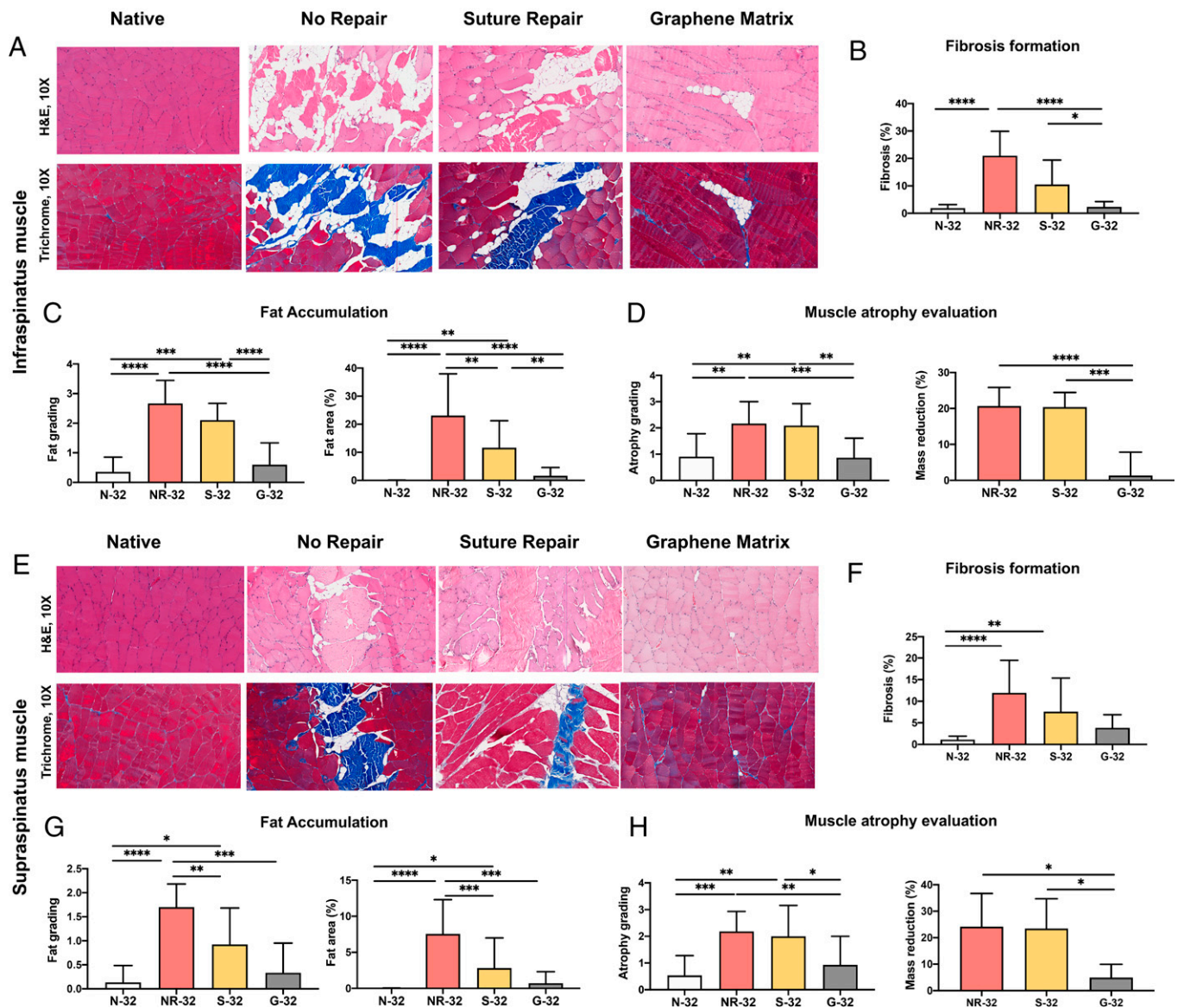


Fig. 6. (A) Representative histological images of infraspinus muscle at 32 wk. The H&E and trichrome staining of cross-sections of the infraspinus muscles used for the quantification of (B) fibrosis formation, (C) fat accumulation, and (D) muscle atrophy evaluation for different groups at 32 wk. (E) Representative histological images of supraspinus muscle at 32 wk. The H&E and trichrome staining of cross-sections of the supraspinus muscles used for the quantification of (F) fibrosis formation, (G) fat accumulation, and (H) muscle atrophy evaluation for different groups at 32 wk. (* $P \leq 0.05$, ** $P \leq 0.01$, *** $P \leq 0.001$, **** $P \leq 0.0001$).

Physiological Changes of Degenerative Muscle after 32 Weeks in a Rat Chronic MRCT Model. The distribution of different types of MHC (MyHC I and II) in supraspinatus and infraspinus muscles at 32 wk was evaluated by immunostaining. Fig. 7 A and C shows the majority of muscle fibers in native muscle (N-32) are MyHC II (fast muscle fiber). The muscle underwent switching from fast (MyHC II) to slow (MyHC I) fiber type after MRCTs in both supraspinatus and infraspinus muscles. Although suture repair did not alter the expression of MyHC I, this switching backed to the normal (native) muscle following the RC repair with the GnP matrix. The statistical analysis showed significant differences between G-32 and S-32 in infraspinus, as well as G-32 and NR-32 in both muscles, whereas there were no significant differences between N-32 and G-32 (Fig. 7 B and D).

The cross-sectional area of muscle fibers was measured at 32 wk (SI Appendix, Fig. S10). MRCTs induced significant loss

of fiber size and NR-32 showed the smallest size in both supraspinatus and infraspinus muscles. The average fiber size in G-32 showed statistically significant differences compared to that in S-32 and NR-32, while there was no significant difference between N-32 and G-32.

Toxicity Evaluation of GnP Matrix on Different Organs. The histological staining of the internal organs showed no obvious tissue damage, inflammation, toxicological effects, or any material accumulation in the organs at 8 and 16 wk after implantation of the GnP matrix (Fig. 8). The congestion grading showed there are no statistically significant differences between graphene matrix-implanted and nonimplanted groups.

The Efficacy of Reversing Muscle Degeneration on Tendon Healing. The effect of GnP matrix implantation on tendon healing was investigated by the histological staining. The H&E

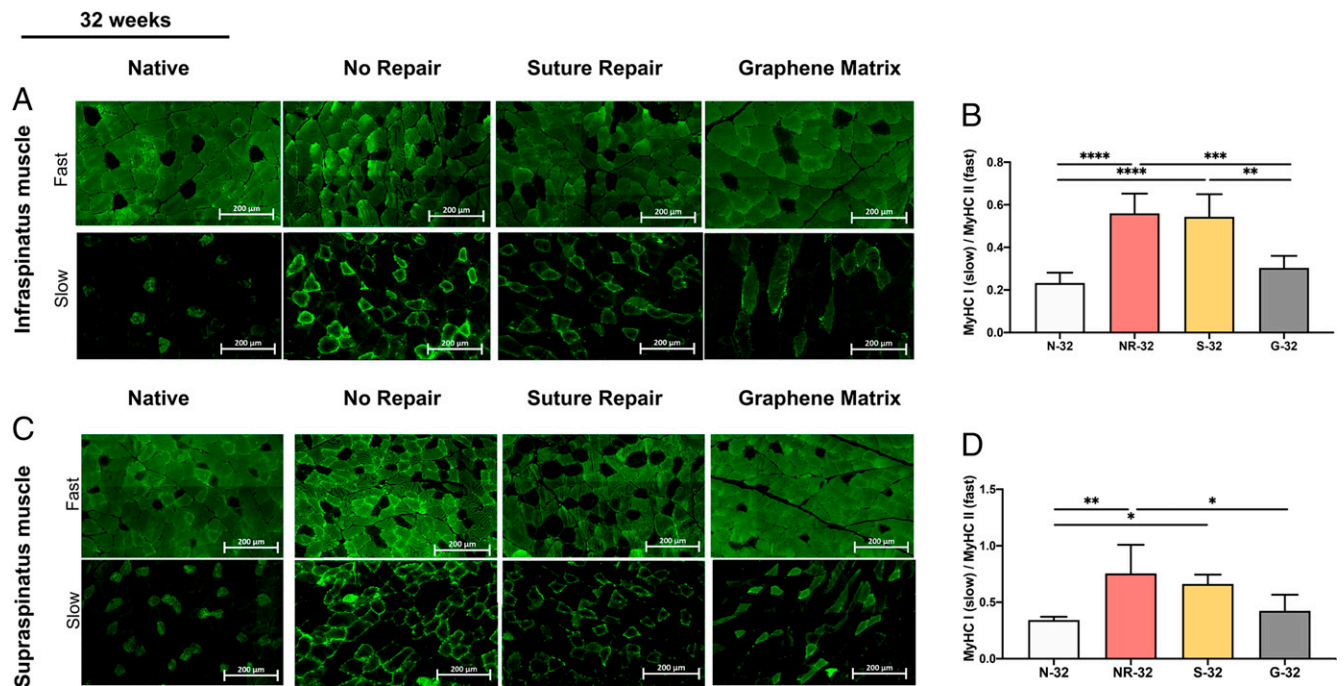


Fig. 7. (A) The immunohistochemistry images of MyHC I (slow), II (fast), and (B) the ratio of MyHC I/MyHC II in infraspinatus muscle at 32 wk for all groups. (C) The immunohistochemistry images of MyHC I and II and (D) the ratio of MyHC I/MyHC II in supraspinatus muscle at 32 wk for all groups. (* $P \leq 0.05$, ** $P \leq 0.01$, *** $P \leq 0.001$, **** $P \leq 0.0001$).

staining of the tendon–bone interface showed that no fibrocartilage zone formation can be observed in S-32. However, the separating line between tendon and bone became partially unclear in G-32. The tendon–bone continuity and regularity can be observed in G-32 (Fig. 9). The expression of glycosaminoglycan (red-stained area in the Safranin O–stained images) at the tendon–bone interface indicated the formation of a new fibrocartilage layer in G-32. The treatment of muscle atrophy and fat accumulation using the GnP matrix exhibited a positive effect on tendon-to-bone insertion maturity compared with NR-32 and S-32. The histology of NR-32 shows the retracted tendon stump (marked with a suture at the time of detachment) and the gap between the humerus and tendon stump. In S-32, the collagen fibers presented an irregular arrangement, and the fibrocartilage layer was not observed in the tendon–bone interface. On the other hand, the chondrocytes in G-32 were almost aligned in rows in the fibrocartilage zone. Moreover, the orientation of collagen fibers was spatially aligned in the tendon. In general, more fibrocartilage zones, oriented cells, and oriented fibers were observed in G-32 compared to other injured groups.

The Efficacy of Reversing Muscle Degeneration on Tendon Tensile Properties. The load-to-failure tests of the tendon were performed to gain insight into the functional effect of the GnP matrix. The most common location of failure for NR-24 and NR-32 was at the enthesis, while all N-24 and N-32 groups failed at the midsubstance. The repair groups (S and G) showed a combination of failure locations with no regular pattern. *SI Appendix, Fig. S11* demonstrates the representative images of both supraspinatus and infraspinatus tendons and the different failure behaviors of the samples.

The biomechanical tests were performed to measure the peak load, stiffness, and Young's modulus of both supraspinatus and infraspinatus tendons. All parameters were significantly lower in all injured groups than in the native group at 24 wk (Fig. 10 *A* and *B*). Similarly, the cross-sectional area of the

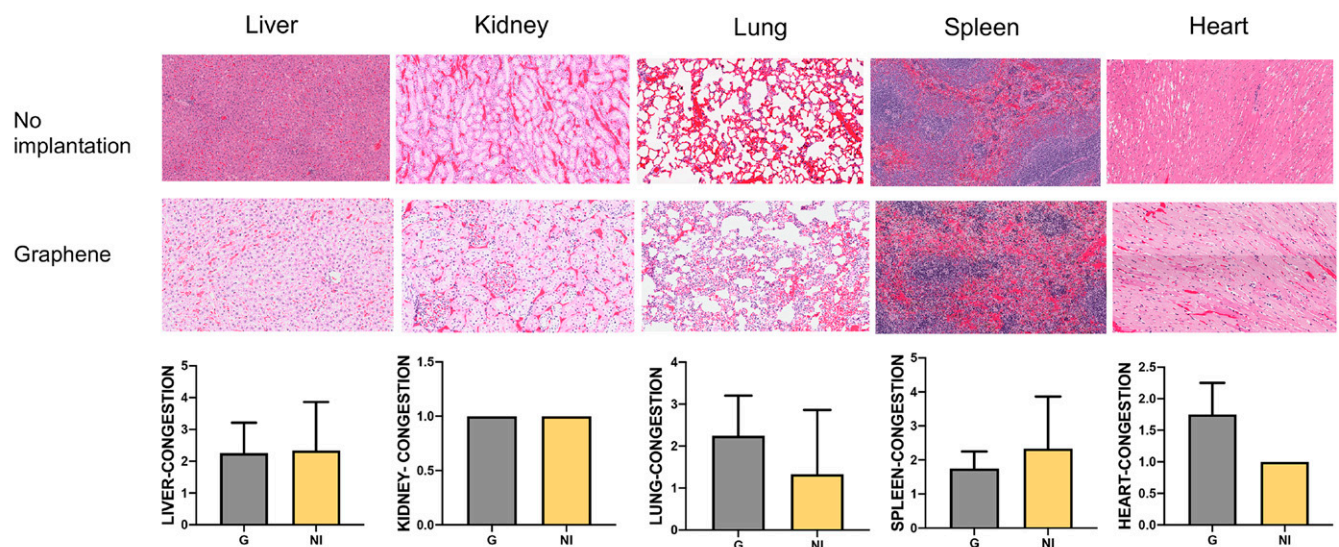
repair site was significantly higher in all injured groups than in the normal tissue. However, G-24 showed a significantly lower cross-sectional area of the supraspinatus tendon and a higher peak load compared to S-24.

At 32 wk, NR-32 and S-32 showed significantly lower peak load and stiffness of both supraspinatus and infraspinatus tendons compared to N-32. However, there are no statistically significant differences between G-32 and N-32. The GnP matrix revealed significant differences compared to NR-32. The significant differences can be observed in the cross-sectional area and Young's modulus of both tendons in N-32 compared to other groups. The cross-sectional area of both supraspinatus and infraspinatus tendons in G-32 was significantly lower than that in S-32. The GnP matrix group demonstrated an overall increase in stiffness, peak load, and Young's modulus compared to NR-32 and S-32 (Fig. 10 *C* and *D*) in both tendons. The differences of tensile properties between G-32 and S-32 were not statistically significant; however, the mechanical test results of G-32 were greater than S-32 in all parameters.

Discussion

In this study, we successfully fabricated the aligned GnP matrix. As indicated in Fig. 1*E*, the alignment of myoblasts along with nanofiber direction suggested that the matrices induced cellular orientation. The aligned orientation of the matrix mimicked the natural structure of muscle tissue, which is composed of highly aligned and long multinucleated myotubes, which provide an essential topographical cue to enhance myoblast growth and differentiation (42, 55, 61, 62). It has been reported that providing a conducive environment under these conditions with no external electrical stimulation can enhance myotube formation and maturation (39, 63). Our GnP matrix showed the synergistic benefit of myoblast differentiation by combining topographical and electrical cues. Myotubes on the GnP matrix showed high differentiation and maturation in both GM and DM. The

Systemic toxicity evaluation (24 weeks)



Systemic toxicity evaluation (32 weeks)

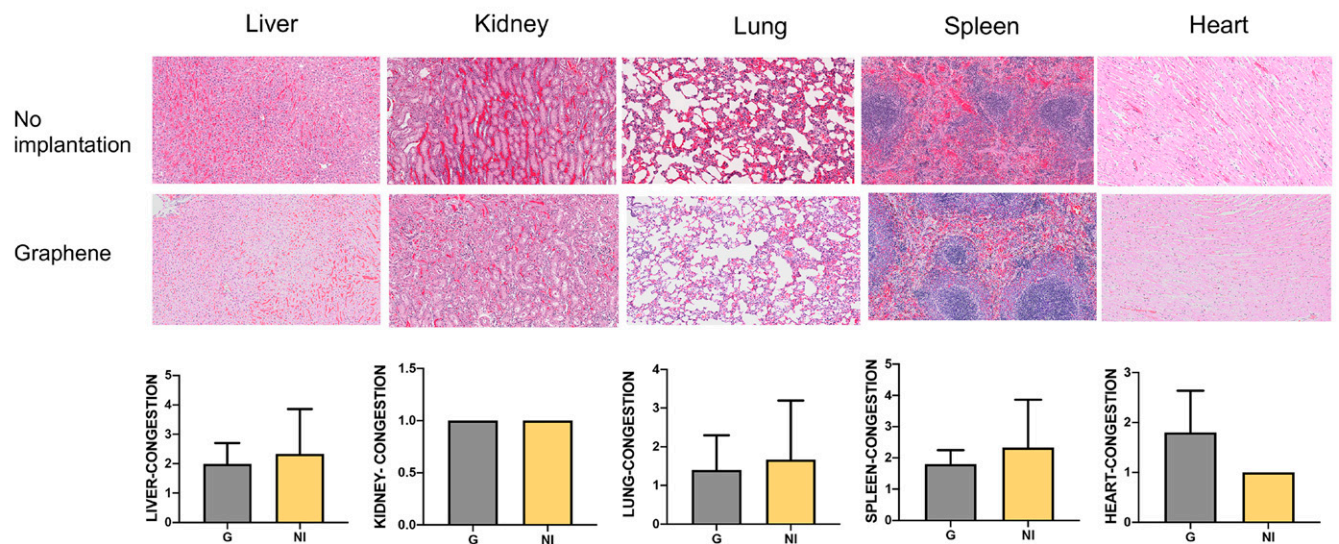


Fig. 8. H&E staining and the congestion grading of the liver, kidney, lung, spleen, and heart of the GnP implanted and nonimplanted groups at 24 and 32 wk.

incorporation of GnP into aligned nanofibers could successfully induce myotube elongation and maturation without the need for changing the environmental conditions of the cell culture. Especially, myoblast cultured on the GnP 1.5 showed the highest values of myotube length ($411.4 \pm 160.8 \mu\text{m}$), fusion ($70.37 \pm 3.044\%$), and maturation indices ($57.59 \pm 7.163\%$) among different GnP concentrations we tested in GM (Fig. 2B). We hence concluded that GnP itself induced myoblast differentiation and myotube formation.

It is important to understand the underlying mechanism of GnP in promoting cell differentiation in the context of understanding its effects on muscle repair and regeneration. It is known that calcium ions play important roles not only in muscle cellular contraction but also in modulating the muscle gene expression through altering the function and localization of transcriptional factors (57, 64, 65). Wang et al. reported a higher concentration of calcium ions of cardiac myoblasts on a conductive matrix (64). We detected the higher intracellular calcium

ion levels of C_2C_{12} myoblasts on the GnP matrix (Fig. 3). It is noted that there is an increase in intracellular calcium level of C_2C_{12} on PLLA matrix in DM. This may be caused by C_2C_{12} myoblast differentiation, which has been reported to express L-type calcium ion channels (57). The calcium levels in the myoblasts were further decreased at day 7. The presence of graphene might have a rapid and short-term effect on increasing the concentration of intracellular calcium ions and its effect gradually reduces. This result is consistent with the enhanced MHC expression, which showed the myotube formation and maturation at day 7 in both GM and DM (Fig. 2A and C). This study demonstrated a correlation between the increased intracellular calcium ion level and the enhanced myotube formation on the GnP matrix. One of the possible explanations for the GnP effect on calcium levels could be its nanostructure. It has been reported that nanometer and submicrometer-sized graphene materials increase the intracellular calcium ions via releasing the calcium ions from internal stores into the cytoplasm (66). However, we

32 weeks, Graphene matrix

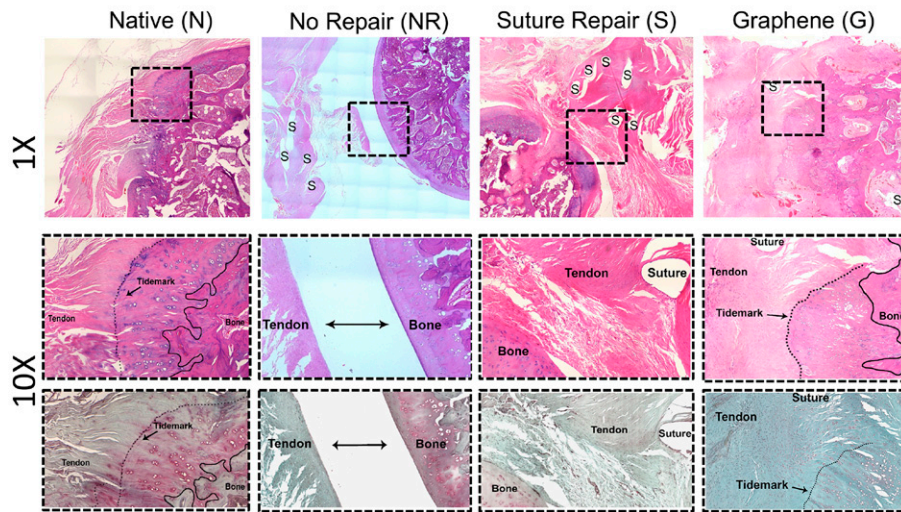


Fig. 9. The representative images of H&E (*Top* and *Middle*) and Safranin O (*Bottom*) staining of the tendon–bone insertion for native, no repair, suture, and GnP matrix at 32 wk following the surgery.

cannot conclude the elevated intracellular calcium level is the only mechanism for the regenerative potential of graphene.

We also confirmed that graphene could suppress lipid production in ADSCs (Fig. 4). These outcomes suggest the inhibitory effect of graphene on adipogenesis. This promising result provides a compelling case for using the graphene matrix in reducing fat formation during RC healing.

Muscle degeneration following massive rotator cuff tendon tears is described by fat accumulation, muscle atrophy, and fibrosis formation in the RC muscles (17, 33, 67–71). In this study, we confirmed a significant increase in fat accumulation, muscle atrophy, and fibrosis formation at 16 wk (NR-16) compared with normal muscles (N-16) (*SI Appendix, Fig. S8*). We utilized a standard grading system to classify the severity of fat accumulation after RCTs, described by Goutallier et al. (67, 72). Clinically a large number of RCTs are in stage 1 or stage 2 (71). Our results are related mostly to grades 1 to 2 of Goutallier’s grading for supraspinatus and grades 2 to 3 for infraspinatus. Consistent with other studies (68, 73), our results showed more severe fat accumulation in the infraspinatus muscle compared to the supraspinatus following the chronic RCT model at 24 and 32 wk. There is no clear explanation for this phenomenon. Since the rate of fibrous of tissues was significantly lower in the supraspinatus muscle compared to the infraspinatus muscle, the severe fat accumulation and fibrosis formation in the infraspinatus could be caused by different levels and distributions of muscle progenitors such as fibro/adipogenic progenitor cells in the muscles.

It is known that current surgical repair cannot reverse fat accumulation and muscle atrophy (9, 74). Patients with moderate/severe fat accumulation and muscle atrophy suffer from a high retear rate after RC repair (9, 74). Similarly, our results showed that suture repair of the tendons alone with no treatment on RC muscles could not effectively reverse the fat accumulation and muscle atrophy (Figs. 5 and 6). However, the implantation of the GnP matrix significantly reduced fat accumulation compared with the suture repair and no repair groups. These results showed that the efficacy of the GnP matrix was enhanced over time from 24 wk to 32 wk in both muscles (*SI Appendix, Table S1*). In addition, muscle atrophy as measured by cross-sectional area and mass reduction were improved by the use of the GnP matrix. The results support

the potential of the GnP matrix to reverse moderate-to-severe muscle atrophy following a chronic RCT.

Fibrosis is one of the main outcomes of most muscle injuries (18, 75). The formation of fibrosis following rotator cuff tears causes the stiffness of skeletal muscle, which increases the tension on RC muscle and subsequently inhibits the repair of chronic RCTs (18). Our observation on fibrosis percentage by Masson’s trichrome staining confirmed the formation of fibrosis following an MRCT in both supraspinatus and infraspinatus muscles (Figs. 5 *B* and *F* and 6 *B* and *F*). The data showed that repairing the torn RC either with or without the matrix implantation can reduce fibrosis. With the GnP matrix implantation, the fibrosis formation was significantly reduced compared with the suture group and the no repair group.

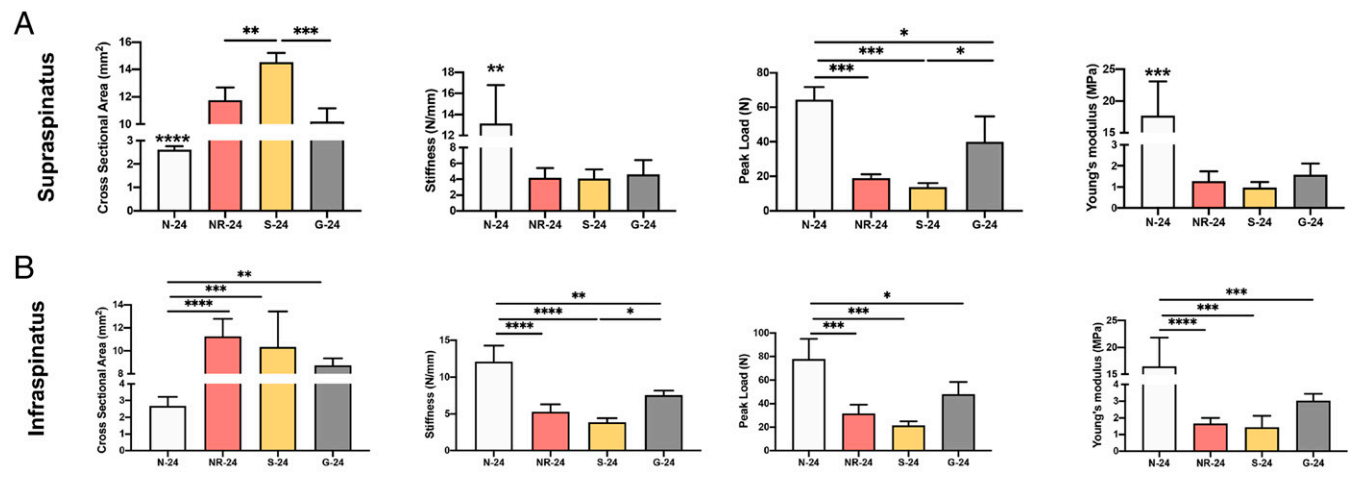
Furthermore, the ratio of muscle fiber types showed that the muscle underwent switching from fast to slow fiber type in NR-32 and S-32. This is consistent with other studies showing the fast-to-slow shift in muscle fiber types following the RCT (73). However, the implantation of the GnP matrix significantly reversed this switching, similar to the normal muscle (N-32) (Fig. 7 *B* and *D*).

The goal of massive rotator cuff tendon tear treatment is to improve tendon morphology and tensile properties. Here, we showed that reversing rotator cuff muscle degeneration is the real key to addressing the real problem. Addressing muscle degeneration can reduce retraction stress on the tendon and improve tendon healing.

The tendon morphology of N-32 showed aligned collagen fibers, which gradually fused into a fibrocartilage zone before reaching the bone (Fig. 9). The tendon-to-bone interface in NR-32 and S-32 was replaced by fibrous scar tissue and the tendon histology showed disorganized collagen with a sudden transition into the bone. G-32 presented the organized collagen and partial formation of the fibrocartilage layer at the tendon–bone interface. Although glycosaminoglycan deposition occurred at the attachment site, we could not observe a consistent reformation of an organized transition zone with calcified and noncalcified fibrocartilage.

It was reported that the high tension, which is required to repair a torn tendon back to the bone in a chronic model, causes a high rate of retear after surgery (76). Moreover, this high tension weakens the biomechanical properties and increases the cross-sectional area of the tendon–bone insertion site (76). However,

24 weeks



32 weeks

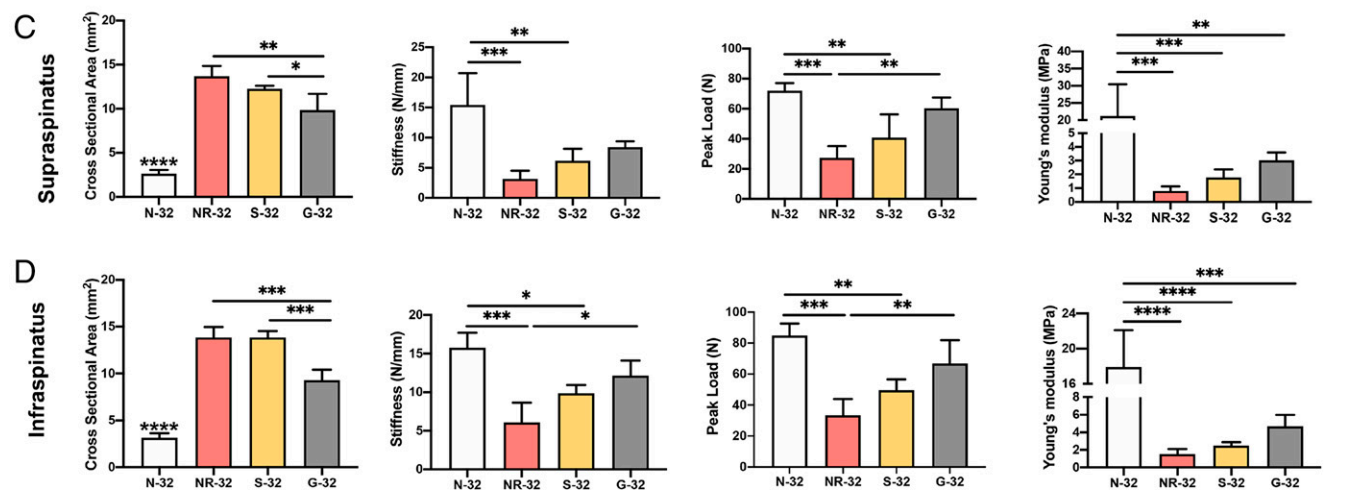


Fig. 10. The results of biomechanical testing, including the tendon cross-sectional area, stiffness, peak load, and Young's modulus of (A) supraspinatus tendon at 24 wk, (B) infraspinatus tendon at 24 wk, (C) supraspinatus tendon at 32 wk, and (D) infraspinatus tendon at 32 wk following the RCTs. (* $P \leq 0.05$, ** $P \leq 0.01$, *** $P \leq 0.001$, **** $P \leq 0.0001$).

reducing fat accumulation and muscle atrophy in G-32, improved the stiffness, peak load, and Young's modulus of both infraspinatus and supraspinatus tendons compared to the no repair and suture repair groups. This treatment can be further developed by involving tendon tissue regeneration strategies together with muscle. The combined treatments of tendon and muscle may be able to have synergistic effects in rotator cuff tendon/muscle healing.

There have been expanding applications of graphene-based materials in the field of biomedical science engineering; therefore, human body exposure to these materials has rapidly increased (66). The evaluations of the safety and biocompatibility of graphene materials on body health are important. Different studies have investigated the biocompatibility of graphene-based materials in vitro and in vivo (44, 77–79). However, the long-term toxicity data have not been widely reported. We evaluated the systemic toxicity of graphene matrix in the rats at 8 and 16 wk after implantation. Our findings have shown no significant health risk, no obvious tissue damage, and no toxicological effects. A mild inflammatory response was observed in the organs after implantation of the GnP matrix. No material accumulation was found in the organs in these experimental conditions.

Conclusion

Massive chronic rotator cuff tendon tears of the shoulder represent a widespread clinical condition that can be highly problematic. We believe that muscle degeneration in chronic massive rotator cuff tears constitutes the real problem that must be addressed. In this study, we reported the efficacy of a unique graphene-based formulation in reversing the degenerative changes of RC muscles. First, we showed that the incorporation of graphene nanoplatelet GnPs into aligned nanofibers significantly increased the myogenic differentiation of C₂C₁₂ myoblasts in vitro. Our work indicates that the significant effects of graphene on myoblasts can be attributed to graphene's ability in enhancing intracellular calcium ions. Also, we showed that the graphene matrix suppressed adipogenesis in ADSCs. This observation provides a promising approach in using this graphene-based matrix to treat and reduce fat accumulation, which is a major challenge in musculotendinous injuries. Further, we found significant effects of the GnP matrix on reducing fat accumulation, muscle atrophy, and fibrosis formation in vivo, implanting the matrix on both supraspinatus and infraspinatus muscles following a chronic MRCT. Our results showed that reducing the

muscle degenerative changes can improve the biomechanical properties of the tendons and subsequently the outcomes of surgery. Furthermore, the histological results of the internal organs confirmed the long-term safety of the GnP matrix in this rat model. These promising results of biocompatibility and the potential of the GnP matrix to treat muscle degeneration provide compelling information for using the GnP matrix in future studies.

Methods

Detailed information is provided in *SI Appendix, Methods*.

GnP Matrix Optimization. Nonfunctionalized GnPs were used in this study, which consist of multilayers of platelet-like graphite nanocrystals with an overall thickness of ~3 to 10 nm (40, 52, 53). To optimize the content of graphene, different concentrations of GnP/PLLA solutions were prepared for electrospinning (*SI Appendix*). The morphology and electrical conductivity were tested. Further, the biocompatibility and differentiation potential of the matrices were investigated upon seeding the matrices with C₂C₁₂ cells in both standard GM and DM. The myoblasts viability and differentiation were investigated using live/dead assays and immunostaining. The cells were imaged with a confocal microscope and the myotube length, fusion index, and maturation index were measured for each group. The fusion index was determined as the percentage of MHC-positive cells with more than two nuclei among the MHC-positive cells (80, 81). The maturation index was calculated as the percentage of myotubes with more than five nuclei (42, 61).

The concentrations that showed higher levels of cell viability, myotube formation, and maturation were selected for the rest of the studies. The effect of graphene on intracellular calcium levels was evaluated using Fluo-4-AM calcium imaging. Besides, the effect of graphene on adipogenic differentiation in ADSCs was investigated in vitro through Oil Red O staining and quantitative analysis. The results of graphene were compared with the PLLA matrix as the control group. The optimized matrix, which showed the highest cell viability and myotube formation and showed the inhibitory effects on adipogenesis was evaluated in a preclinical animal model of chronic MRCTs.

Animal Study Design. All animal experiments were performed following protocols approved by the Institutional Animal Care and Use Committee at the University of Connecticut. In order to create the chronic injury model of massive full-thickness RCTs, we used the standard time point of 16 wk. To show the competence of the time point, the model was developed using 12 male Sprague-Dawley rats (11 wk old, Charles River Laboratories, Inc.). The massive full-thickness injury was created on both supraspinatus and infraspinatus tendons in the left shoulder. The rats were killed after 16 wk and evaluated in terms of muscle degenerative changes (*SI Appendix, Fig. S8*). Following the development of the model, 72 male Sprague-Dawley rats (11 wk old, Charles River Laboratories, Inc.) were utilized for the study where the left shoulders were used for the experimental groups and the right shoulders were used as native control groups. At 16 wk after the injury, 48 rats were randomly selected for the repair

procedure. The 24 remaining rats were used as the no repair control groups. The suture surgical techniques were performed on 48 selected rats to repair both tendons. Half of the rats were randomly selected for GnP matrix implantation on the muscles following the tendon repair. The matrices were transplanted on the supraspinatus and infraspinatus muscles. Rats were killed, and tissues were harvested at 24 and 32 wk after the initial injury for analysis (equal to 8 and 16 wk after the matrix implantation in the repair groups). Harvested muscles were imaged and characterized using immunohistochemistry, H&E, and Masson's trichrome histology. The muscle atrophy was evaluated using wet weight measurement, muscle atrophy grading, muscle cross-sectional area quantification, and immunohistochemistry analysis of MHC I and MHC II as mentioned in *SI Appendix* (17, 71–73, 82, 83). The fat accumulation was evaluated using a grading system and fat area quantification. The degree of fibrosis was measured as the area of collagen staining fibers divided by the total area of the image after trichrome staining. Internal organs were imaged and characterized using H&E and the tendon-bone tissues were harvested for biomechanics and histological assessment.

Statistical Analysis. The unpaired Student's *t* test was used to compare between two groups. One-way analysis of variance (ANOVA) was used to analyze the comparison among more than two groups. The significant differences in groups were determined by Dunn, Dunnett, Sidak, and Tukey pairwise comparison tests. If the data failed the normality test, a Kruskal-Wallis test with Dunn's multiple comparisons was run to compare the groups; otherwise, one-way ANOVA with Tukey's or Sidak's multiple comparisons test was used. The data are expressed as means ± SD and the difference of *P* < 0.05 was considered statistically significant.

Data Availability. All study data are included in the article and/or supporting information.

ACKNOWLEDGMENTS. We thank Dr. Zhifang Hao, Ion Jackman, and Dr. David Rowe for their help with the muscle and tendon histology. We thank Dr. Aneesah McClinton and the Center for Comparative Medicine for the animal surgery training and performance. This work was funded by Department of Health and Human Services (DHHS)/NIH/National Institute of Arthritis & Musculoskeletal & Skin Diseases (NIAMS) entitled, Regenerative Engineering of Complex Musculoskeletal Tissue and Joints, Grant No. DP1AR068147 and NSF/Emerging Frontiers in Research and Innovation program (EFRI) Grant No. 1332329.

Author affiliations: ^aConnecticut Convergence Institute for Translation in Regenerative Engineering, University of Connecticut Health, Farmington, CT 06030; ^bRaymond and Beverly Sackler Center for Biomedical, Biological, Physical, and Engineering Sciences, University of Connecticut Health Center, Farmington, CT 06030; ^cDepartment of Biomedical Engineering, University of Connecticut, Storrs, CT 06269; ^dDepartment of Orthopedic Surgery, University of Connecticut Health Center, Farmington, CT 06030; ^eDepartment of Pathobiology and Veterinary Science, University of Connecticut, Storrs, CT 06269; ^fConnecticut Veterinary Medical Diagnostic Laboratory, Storrs, CT; ^gDepartment of Materials Science and Engineering, University of Connecticut, Storrs, CT 06269; and ^hDepartment of Chemical and Biomolecular Engineering, University of Connecticut, Storrs, CT 06269

1. K. J. Cronin *et al.*, Increased health care costs and opioid use in patients with anxiety and depression undergoing rotator cuff repair. *Arthroscopy* **36**, 2655–2660 (2020).
2. E. M. Marigi *et al.*, Cost analysis and complication rate comparing open, mini-open, and all arthroscopic rotator cuff repair. *JSES Rev. Rep. Tech.* **1**, 84–89 (2021).
3. J. E. Hsu, J. G. Horneff, A. O. Gee, Immobilization after rotator cuff repair: What evidence do we have now? *Orthop. Clin. North Am.* **47**, 169–177 (2016).
4. S. S. Novakova *et al.*, Tissue-engineered tendon constructs for rotator cuff repair in sheep. *J. Orthop. Res.* **36**, 289–299 (2018).
5. N. B. Jain *et al.*, Epidemiology of musculoskeletal upper extremity ambulatory surgery in the United States. *BMC Musculoskelet. Disord.* **15**, 4 (2014).
6. B. J. Kelly, L. D. Field, Arthroscopic repair of medial transtendinous rotator cuff tears. *Arthrosc. Tech.* **6**, e2217–e2221 (2017).
7. S. Patel, A. P. Gualtieri, H. H. Lu, W. N. Levine, Advances in biologic augmentation for rotator cuff repair. *Ann. N. Y. Acad. Sci.* **1383**, 97–114 (2016).
8. B. B. Rothrauff *et al.*, The rotator cuff organ: Integrating developmental biology, tissue engineering, and surgical considerations to treat chronic massive rotator cuff tears. *Tissue Eng. Part B Rev.* **23**, 318–335 (2017).
9. O. Agha *et al.*, Rotator cuff tear degeneration and the role of fibro-adipogenic progenitors. *Ann. N. Y. Acad. Sci.* **1490**, 13–28 (2021).
10. S. Wu, Y. Wang, P. N. Streubel, B. Duan, Living nanofiber yarn-based woven biotextiles for tendon tissue engineering using cell tri-culture and mechanical stimulation. *Acta Biomater.* **62**, 102–115 (2017).
11. M. J. Smetana, P. Moncada-Larrotiz, E. M. Arruda, A. Bedi, L. M. Larkin, Tissue-engineered tendon for enthesis regeneration in a rat rotator cuff model. *Biores. Open Access* **6**, 47–57 (2017).
12. D. Kovacevic, S. A. Rodeo, Biological augmentation of rotator cuff tendon repair. *Clin. Orthop. Relat. Res.* **466**, 622–633 (2008).
13. T. Thangarajah *et al.*, Supraspinatus detachment causes musculotendinous degeneration and a reduction in bone mineral density at the enthesis in a rat model of chronic rotator cuff degeneration. *Shoulder Elbow* **9**, 178–187 (2017).
14. J. A. Gimbel *et al.*, Supraspinatus tendon organizational and mechanical properties in a chronic rotator cuff tear animal model. *J. Biomech.* **37**, 739–749 (2004).
15. B. Mierzejewski *et al.*, "Human and mouse skeletal muscle stem and progenitor cells in health and disease" in *Seminars in Cell & Developmental Biology* (Elsevier, 2020), pp. 93–104.
16. E. Frey *et al.*, Adipogenic and myogenic gene expression in rotator cuff muscle of the sheep after tendon tear. *J. Orthop. Res.* **27**, 504–509 (2009).
17. X. Tang *et al.*, The treatment of muscle atrophy after rotator cuff tears using electroconductive nanofibrous matrices. *Regen. Eng. Transl. Med.* **7**, 1–9 (2021).
18. X. Liu *et al.*, Investigating the cellular origin of rotator cuff muscle fatty infiltration and fibrosis after injury. *Muscles Ligaments Tendons J.* **6**, 6–15 (2016).
19. J. M. Grasman, M. J. Zayas, R. L. Page, G. D. Pins, Biomimetic scaffolds for regeneration of volumetric muscle loss in skeletal muscle injuries. *Acta Biomater.* **25**, 2–15 (2015).
20. N. Matthias *et al.*, Volumetric muscle loss injury repair using in situ fibrin gel cast seeded with muscle-derived stem cells (MDSCs). *Stem Cell Res. (Amst.)* **27**, 65–73 (2018).

21. Z. Zhang, L. H. Klausen, M. Chen, M. Dong, Electroactive scaffolds for neurogenesis and myogenesis: Graphene-based nanomaterials. *Small* **14**, e1801983 (2018).
22. S. Beeler, E. T. Ek, C. Gerber, A comparative analysis of fatty infiltration and muscle atrophy in patients with chronic rotator cuff tears and suprascapular neuropathy. *J. Shoulder Elbow Surg.* **22**, 1537–1546 (2013).
23. C. Gerber, B. Fuchs, J. Hodler, The results of repair of massive tears of the rotator cuff. *J. Bone Joint Surg. Am.* **82**, 505–515 (2000).
24. Y. S. Lee, J. Y. Jeong, C.-D. Park, S. G. Kang, J. C. Yoo, Evaluation of the risk factors for a rotator cuff retear after repair surgery. *Am. J. Sports Med.* **45**, 1755–1761 (2017).
25. S. Yokoya, Y. Mochizuki, Y. Nagata, M. Deie, M. Ochi, Tendon-bone insertion repair and regeneration using polyglycolic acid sheet in the rabbit rotator cuff injury model. *Am. J. Sports Med.* **36**, 1298–1309 (2008).
26. A. Lädermann *et al.*, Classification of full-thickness rotator cuff lesions: A review. *EFORT Open Rev.* **1**, 420–430 (2017).
27. S. Zhao *et al.*, Biomaterials based strategies for rotator cuff repair. *Colloids Surf. B Biointerfaces* **157**, 407–416 (2017).
28. F. Saadat, A. C. Deymier, V. Birman, S. Thomopoulos, G. M. Genin, The concentration of stress at the rotator cuff tendon-to-bone attachment site is conserved across species. *J. Mech. Behav. Biomed. Mater.* **62**, 24–32 (2016).
29. D. Kovacevic *et al.*, Calcium-phosphate matrix with or without TGF- β 3 improves tendon-bone healing after rotator cuff repair. *Am. J. Sports Med.* **39**, 811–819 (2011).
30. H. Shimokobe *et al.*, Risk factors for retear of large/massive rotator cuff tears after arthroscopic surgery: An analysis of tearing patterns. *J. Orthop. Surg. Res.* **12**, 140 (2017).
31. T. Thangarajah *et al.*, Augmentation of rotator cuff repair with soft tissue scaffolds. *Orthop. J. Sports Med.* **3**, 2325967115587495 (2015).
32. S. Gumina, M. Borroni, "Classifications of the rotator cuff tears" in *Rotator Cuff Tear: Pathogenesis, Evaluation and Treatment*, S. Gumina, Ed. (Springer International Publishing, Cham, 2017), pp. 123–131.
33. N. Seivias *et al.*, Mesenchymal stem cell secretome improves tendon cell viability in vitro and tendon-bone healing in vivo when a tissue engineering strategy is used in a rat model of chronic massive rotator cuff tear. *Am. J. Sports Med.* **46**, 449–459 (2018).
34. I. K. Y. Lo, S. S. Burkhart, Arthroscopic repair of massive, contracted, immobile rotator cuff tears using single and double interval slides: Technique and preliminary results. *Arthroscopy* **20**, 22–33 (2004).
35. D. Li *et al.*, Fabrication of multilayered nanofiber scaffolds with a highly aligned nanofiber yarn for anisotropic tissue regeneration. *ACS Omega* **5**, 24340–24350 (2020).
36. C. Liu *et al.*, Controllable aligned nanofiber hybrid yarns with enhanced bioproperties for tissue engineering. *Macromol. Mater. Eng.* **304**, 1900089 (2019).
37. Y. Wu, Y. Han, Y. S. Wong, J. Y. H. Fuh, Fibre-based scaffolding techniques for tendon tissue engineering. *J. Tissue Eng. Regen. Med.* **12**, 1798–1821 (2018).
38. N. Saveh-Shemshaki, L. S. Nair, C. T. Laurencin, Nanofiber-based matrices for rotator cuff regenerative engineering. *Acta Biomater.* **94**, 64–81 (2019).
39. X. Zhang, N. Saveh-Shemshaki, H.-M. Kan, Y. Khan, C. T. Laurencin, Biomimetic Electroconductive Nanofibrous Matrices for Skeletal Muscle Regenerative Engineering. *Regen. Eng. Transl. Med.* **6**, 228–237 (2020).
40. N. S. Shemshaki, C. Laurencin, "Graphene-based nanofibers for skeletal muscle tissue regeneration." Google Patents (2021).
41. Y. Li *et al.*, Engineering cell alignment in vitro. *Biotechnol. Adv.* **32**, 347–365 (2014).
42. M.-C. Chen, Y.-C. Sun, Y.-H. Chen, Electrically conductive nanofibers with highly oriented structures and their potential application in skeletal muscle tissue engineering. *Acta Biomater.* **9**, 5562–5572 (2013).
43. K. Metavarayuth, P. Sitasuwan, X. Zhao, Y. Lin, Q. Wang, Influence of surface topographical cues on the differentiation of mesenchymal stem cells in vitro. *ACS Biomater. Sci. Eng.* **2**, 142–151 (2016).
44. S. R. Shin *et al.*, Graphene-based materials for tissue engineering. *Adv. Drug Deliv. Rev.* **105**, 255–274 (2016).
45. Y. Du, J. Ge, Y. Li, P. X. Ma, B. Lei, Biomimetic elastomeric, conductive and biodegradable polycitrate-based nanocomposites for guiding myogenic differentiation and skeletal muscle regeneration. *Biomaterials* **157**, 40–50 (2018).
46. M. Mahmoudifard *et al.*, The different fate of satellite cells on conductive composite electrospun nanofibers with graphene and graphene oxide nanosheets. *Biomed. Mater.* **11**, 025006 (2016).
47. S. B. Jo *et al.*, Nano-graphene oxide/polyurethane nanofibers: Mechanically flexible and myogenic stimulating matrix for skeletal tissue engineering. *J. Tissue Eng.* **11**, 2041731419900424 (2020).
48. R. Rauti *et al.*, Graphene oxide nanosheets reshape synaptic function in cultured brain networks. *ACS Nano* **10**, 4459–4471 (2016).
49. A. Fabbro *et al.*, Graphene-based interfaces do not alter target nerve cells. *ACS Nano* **10**, 615–623 (2016).
50. S. W. Hong *et al.*, Enhanced neural cell adhesion and neurite outgrowth on graphene-based biomimetic substrates. *BioMed Res. Int.* **2014**, 212149 (2014).
51. A. J. Ryan *et al.*, Electroconductive biohybrid collagen/pristine graphene composite biomaterials with enhanced biological activity. *Adv. Mater.* **30**, e1706442 (2018).
52. Anonymous, Graphene Nanoplatelets Non Functionalized. <https://www.cheaptubes.com/product/graphene-nanoplatelets-non-functionalized>.
53. M.-Y. Shen *et al.*, Mechanical properties and tensile fatigue of graphene nanoplatelets reinforced polymer nanocomposites. *J. Nanomater.* **2013**, 565401 (2013).
54. V. Palmieri, F. Sciandra, M. Bozzi, M. De Spirito, M. Papi, 3D graphene scaffolds for skeletal muscle regeneration: Future perspectives. *Front. Bioeng. Biotechnol.* **8**, 383 (2020).
55. H. S. Yang *et al.*, Electroconductive nanopatterned substrates for enhanced myogenic differentiation and maturation. *Adv. Healthc. Mater.* **5**, 137–145 (2016).
56. M. Gajendiran *et al.*, Conductive biomaterials for tissue engineering applications. *J. Ind. Eng. Chem.* **51**, 12–26 (2017).
57. G. A. Porter Jr., R. F. Makuck, S. A. Rivkees, Reduction in intracellular calcium levels inhibits myoblast differentiation. *J. Biol. Chem.* **277**, 28942–28947 (2002).
58. D. M. Pedrotty *et al.*, Engineering skeletal myoblasts: Roles of three-dimensional culture and electrical stimulation. *Am. J. Physiol. Heart Circ. Physiol.* **288**, H1620–H1626 (2005).
59. A. Bianco *et al.*, *All in the Graphene Family—A Recommended Nomenclature for Two-Dimensional Carbon Materials* (Elsevier, 2013).
60. E. Luong-Van, T. T. Madanagopal, V. Rosa, Mechanisms of graphene influence on cell differentiation. *Mater. Today Chem.* **16**, 100250 (2020).
61. S. H. Ku, S. H. Lee, C. B. Park, Synergic effects of nanofiber alignment and electroactivity on myoblast differentiation. *Biomaterials* **33**, 6098–6104 (2012).
62. T. M. Uehara *et al.*, Fabrication of random and aligned electrospun nanofibers containing graphene oxide for skeletal muscle cells scaffold. *Polym. Adv. Technol.* **31**, 1437–1443 (2020).
63. H. Y. Gong *et al.*, A novel conductive and micropatterned PEG-based hydrogel enabling the topographical and electrical stimulation of myoblasts. *ACS Appl. Mater. Interfaces* **11**, 47695–47706 (2019).
64. Y. Wang *et al.*, Intracellular calcium ions and morphological changes of cardiac myoblasts response to an intelligent biodegradable conducting copolymer. *Mater. Sci. Eng. C* **90**, 168–179 (2018).
65. E. J. Lee, J. H. Nam, I. Choi, Fibromodulin modulates myoblast differentiation by controlling calcium channel. *Biochem. Biophys. Res. Commun.* **503**, 580–585 (2018).
66. M.-H. Lim *et al.*, Graphene oxide induces apoptotic cell death in endothelial cells by activating autophagy via calcium-dependent phosphorylation of c-Jun N-terminal kinases. *Acta Biomater.* **46**, 191–203 (2016).
67. D. Goutallier, J.-M. Postel, P. Gleyze, P. Leguilloux, S. Van Driessche, Influence of cuff muscle fatty degeneration on anatomic and functional outcomes after simple suture of full-thickness tears. *J. Shoulder Elbow Surg.* **12**, 550–554 (2003).
68. N. Seivias *et al.*, Animal model for chronic massive rotator cuff tear: Behavioural and histologic analysis. *Knee Surg. Sports Traumatol. Arthrosc.* **23**, 608–618 (2015).
69. N. Seivias *et al.*, Mesenchymal stem cell secretome: A potential tool for the prevention of muscle degenerative changes associated with chronic rotator cuff tears. *Am. J. Sports Med.* **45**, 179–188 (2017).
70. K. S. Washington, N. S. Shemshaki, C. T. Laurencin, The role of nanomaterials and biological agents on rotator cuff regeneration. *Regen. Eng. Transl. Med.* **7**, 440–449 (2021).
71. M. A. Abdou *et al.*, How long should we wait to create the goutallier stage 2 fatty infiltrations in the rabbit shoulder for repairable rotator cuff tear model? *BioMed Res. Int.* **2019**, 7387131 (2019).
72. D. Goutallier, J.-M. Postel, J. Bernageau, L. Lavau, M.-C. Voisin, Fatty muscle degeneration in cuff ruptures. Pre- and postoperative evaluation by CT scan. *Clin. Orthop. Relat. Res.* **304**, 78–83 (1994).
73. H. M. Kim, L. M. Galatz, C. Lim, N. Havlioglu, S. Thomopoulos, The effect of tear size and nerve injury on rotator cuff muscle fatty degeneration in a rodent animal model. *J. Shoulder Elbow Surg.* **21**, 847–858 (2012).
74. J. N. Gladstone, J. Y. Bishop, I. K. Lo, E. L. Flatow, Fatty infiltration and atrophy of the rotator cuff do not improve after rotator cuff repair and correlate with poor functional outcome. *Am. J. Sports Med.* **35**, 719–728 (2007).
75. A. Lebaschi *et al.*, Animal models for rotator cuff repair. *Ann. N. Y. Acad. Sci.* **1383**, 43–57 (2016).
76. J. A. Gimbel, J. P. Van Kleunen, S. P. Lake, G. R. Williams, L. J. Soslowsky, The role of repair tension on tendon to bone healing in an animal model of chronic rotator cuff tears. *J. Biomech.* **40**, 561–568 (2007).
77. J. K. Kim *et al.*, 28-Day inhalation toxicity of graphene nanoplatelets in Sprague-Dawley rats. *Nanotoxicology* **10**, 891–901 (2016).
78. M. C. P. Mendonça *et al.*, Reduced graphene oxide: Nanotoxicological profile in rats. *J. Nanobiotechnology* **14**, 53 (2016).
79. A. Schinwald *et al.*, Minimal oxidation and inflammogenicity of pristine graphene with residence in the lung. *Nanotoxicology* **8**, 824–832 (2014).
80. Y. Zhang, Z. Zhang, Y. Wang, Y. Su, M. Chen, 3D myotube guidance on hierarchically organized anisotropic and conductive fibers for skeletal muscle tissue engineering. *Mater. Sci. Eng. C* **116**, 111070 (2020).
81. N. Sangaj *et al.*, Heparin mimicking polymer promotes myogenic differentiation of muscle progenitor cells. *Biomacromolecules* **11**, 3294–3300 (2010).
82. X. Tang, "Electroconductive nanofiber matrices for muscle regeneration" in *Materials Science and Engineering* (University of Connecticut, 2018).
83. C. Lee *et al.*, Beige fibro-adipogenic progenitor transplantation reduces muscle degeneration and improves function in a mouse model of delayed repair of rotator cuff tears. *J. Shoulder Elbow Surg.* **29**, 719–727 (2020).